Proceedings of the ASME 2010 3rd Joint US-European Fluids Engineering Summer Meeting and 8th International Conference on Nanochannels, Microchannels, and Minichannels
FEDSM-ICNMM2010
August 1-5, 2010, Montreal, Canada

FEDSM-ICNMM2010-30438

LARGE-AMPLITUDE OSCILLATIONS OF A FINITE-THICKNESS CANTILEVERED FLEXIBLE PLATE IN VISCOUS CHANNEL FLOW

Novak S. J. Elliott*
Fluid Dynamics Research Group
Curtin University of Technology
GPO Box U1987, Perth, WA
Australia
Email: n.s.j.elliott@curtin.edu.au

Anthony D. Lucey
Fluid Dynamics Research Group
Curtin University of Technology
GPO Box U1987, Perth, WA
Australia
Email: t.lucey@curtin.edu.au

Matthias Heil
School of Mathematics
University of Manchester
Oxford Road, Manchester, M139PL
United Kingdom
Email: m.heil@maths.man.ac.uk

ABSTRACT

The broad aim of the present work is to elucidate mechanisms of obstructive breathing disorders (snoring, sleep apnea) in which flow-induced instabilities of the soft palate feature. We use the well-established analogue system model wherein a two-dimensional flexible plate (soft palate) is mounted downstream of a rigid surface that separates upper and lower plane channel (oral and nasal tracts) flows that interact with the plate motion and then combine into a single plane channel (pharynx) flow. For this system, we take the next step towards biomechanical realism by modeling finite-amplitude motions of the flexible plate and incorporating finite thickness in its structure. The structural model makes use of a geometrically nonlinear formulation of the solid mechanics. Viscous flow is modeled at Reynolds numbers giving unsteady laminar flow. The fully-coupled fluid-structure interaction (FSI) model is developed using the open-source finite-element library `oomph-lib`. We first show the effects of finite amplitude and finite thickness on the in-vacuo modes of the plate through a validation study of the structural mechanics. Thereafter, we use the FSI model to illustrate both stable and unstable motions of the plate. Overall, this paper demonstrates the versatility of the new modeling approach and its suitability for characterizing the dependence of the plate's stability on the system parameters.

INTRODUCTION

A cantilevered flexible plate immersed in a two-dimensional channel flow has previously been shown to capture fluid-structure interactions (FSIs) representative of respiratory flow and soft-palate motion in the upper airway [1–5]. In these, and the present study, the analogue FSI system can be represented by Fig. 1. These models generally utilize ideal flow giving very high Reynolds numbers with viscous boundary-layer effects implicitly modeled through the imposition of a Kutta condition [2,4,5] or an applied channel resistance [3]. Recently investigators have modeled the effects of fluid viscosity explicitly for the laminar regime of Reynolds numbers [6] and implemented constant pressure-drop boundary conditions [7]. In all of these studies—across the low-to-high range of Reynolds numbers—short plates (with low mass ratio) are shown to lose their stability to a single-mode flutter instability at a critical value of flow speed or Reynolds number based on channel height. The destabilization mechanism is fundamentally similar being due to an irreversible energy transfer from fluid to plate. This arises from a phase difference between fluid pressure and plate motion that owes its origin to the finite length of the flexible plate [5,6,8].

In all of the aforementioned studies, linear structural mechanics were adopted by using the one-dimensional (1-d) Euler-Bernoulli beam equation. A nonlinear structural model has been developed by including an inextensibility condition but this utilized potential flow [9]. Plainly the soft palate undergoes dis-

*Address all correspondence to this author.

placements beyond the linear range, particularly during obstructive breathing disorders. It is also of non-negligible thickness and is subjected to fluid friction in a viscous flow field. Accordingly, the present work includes these effects and thereby yields a more faithful biomechanical FSI model. To achieve this, we employ a continuum mechanics approach, developing and utilizing a model of the cantilever as a two-dimensional (2-d) elastic solid beam immersed in viscous flowing fluid. As an intermediate step we also implement a (geometrically) nonlinear 1-d beam model. This paper describes the development of the improved FSI model and then demonstrates its utility in simulating both stable and unstable motions of the flexible plate and the characterization of the system's behavior

METHOD

Theoretical model

The system investigated for the case of the 2-d flexible plate is shown schematically in Fig. 1(a). All of the annotated quantities are dimensional, indicated by their superscripted asterisks—we drop the asterisk when referring to a nondimensional quantity. A two-dimensional channel of height H^* and length L^* conveys a fluid of density ρ_f^* and dynamic viscosity μ^* and is divided at the upstream end by a rigid wall of length l_{rigid}^* and thickness h^*, offset from the lower channel wall by a vertical distance Y_0^*, to which a flexible cantilevered plate (length l_{flexible}^* and identical thickness) is attached. Steady Poiseuille flow with mean velocities U_1^* and U_2^* are imposed at inlets 1 (upper) and 2 (lower), respectively, and the outflow is assumed to be parallel and axially traction-free. The flexible plate is modeled as a 2-d elastic solid beam with density ρ_s^*, elastic modulus E^* and Poisson's ratio ν. To examine the effects of asymmetry we set $Y_0^* = H^*/2$ and $U_1^* = U_2^* = U^*$. For the analogous model with a 1-d beam the central rigid wall and beam coincide with the centerline of their 2-d counterparts.

Governing equations

We now describe the equations governing the deformation of the cantilevered flexible plate, the flow of the immersing fluid and their interaction. We begin with the simpler *in vacuo* case before introducing the fluid, and in each case we present the equations for the 1-d beam model ahead of the 2-d beam model. The constitutive law, boundary and initial conditions are treated separately. All equations are presented in nondimensional form, variously making use of characteristic scales of length, $\mathcal{L}^*$, time, $\mathcal{T}^*$, material stress, $\mathcal{S}^*$, fluid pressure, $\mathcal{P}^*$, and fluid velocity, $\mathcal{V}^*$.

In vacuo For the 1-d beam model we nondimensionalize all lengths and spatial coordinates on the beam length, $\mathcal{L}^* = l_{\text{flexible}}^*$, and all stresses and tractions on the effective 1-d

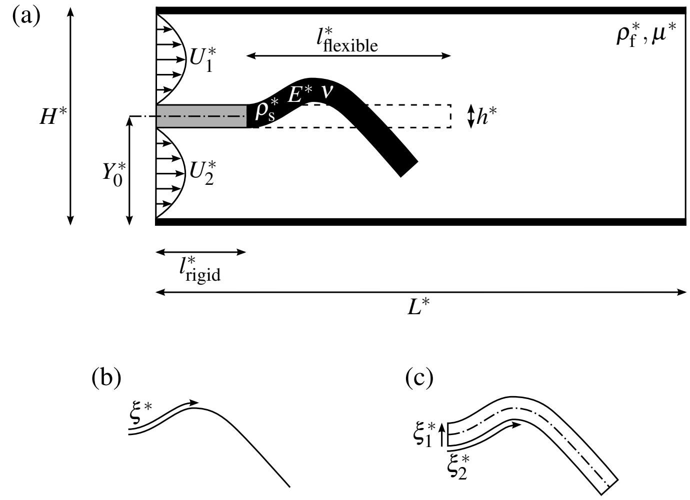

FIGURE 1. SCHEMATIC OF THE FSI SYSTEM INDICATING (a) THE PHYSICAL QUANTITIES OF THE PROBLEM AND THE LAGRANGIAN COORDINATES OF THE (b) 1-D AND (c) 2-D FLEXIBLE PLATE.

elastic modulus, $\mathcal{S}^* = E_{\text{eff}}^* = E^*/(1-\nu^2)$. The beam's undeformed shape is parameterized by a nondimensional Lagrangian coordinate $\xi = \xi^*/l_{\text{flexible}}^*$ [see Fig. 1(b)] so that the nondimensional position vector to a material particle on the beam's centerline in the undeformed configuration is given by $\mathbf{r}(\xi)$. We denote the unit normal to the beam's undeformed centerline by $\hat{\mathbf{n}}$. Applying a traction $\mathbf{T} = \mathbf{T}*/E_{\text{eff}}^*$ (a force per unit deformed length of the beam) deforms the beam, causing its material particles to be displaced to their new positions $\mathbf{R}(\xi)$; the unit normal to the beam's deformed centerline is $\hat{\mathbf{N}}$.

The *principle of virtual displacements* (PVD) governs the beam's deformation, which in nondimensional form is

$$\int_0^{l_{\text{flexible}}} \left[\gamma\,\delta\gamma + \frac{h^2}{12}\kappa\,\delta\kappa - \left(\frac{1}{h}\sqrt{\frac{A}{a}}\,\mathbf{T} - \Lambda^2 \frac{\partial^2 \mathbf{R}}{\partial t^2} \right) \cdot \delta\mathbf{R} \right] \mathrm{d}s = 0, \tag{1}$$

where

$$a = \frac{\partial \mathbf{r}}{\partial \xi} \cdot \frac{\partial \mathbf{r}}{\partial \xi} \quad \text{and} \quad A = \frac{\partial \mathbf{R}}{\partial \xi} \cdot \frac{\partial \mathbf{R}}{\partial \xi} \tag{2a,b}$$

represent the squares of the lengths of infinitesimal material line elements in the undeformed and the deformed configurations, respectively. These may also be interpreted as the '1×1 metric tensors' of the beam's centerline in the respective configurations. The quantity $\sqrt{A/a}$ represents the 'extension ratio' of the beam's centerline, and $\mathrm{d}s = \sqrt{a}\,\mathrm{d}\xi$.

We represent the curvature of the beam's centerline before and after the deformation by

$$b=\hat{\mathbf{n}}\cdot\frac{\partial^2\mathbf{r}}{d\xi^2}\quad\text{and}\quad B=\hat{\mathbf{N}}\cdot\frac{\partial^2\mathbf{R}}{d\xi^2} \tag{3a,b}$$

respectively. The ('1×1') strain and bending 'tensors' γ and κ are then given by

$$\gamma=\frac{1}{2}(A-a)\quad\text{and}\quad \kappa=-(B-b)\,. \tag{4a,b}$$

Thus (1) is a 1-d beam equation that takes into account curvature hence finite length, and axial stretching. Finally,

$$\Lambda=\frac{l^*_{\text{flexible}}}{\mathcal{T}^*}\sqrt{\frac{\rho^*_{\text{s}}}{E^*_{\text{eff}}}} \tag{5}$$

is the ratio of the natural timescale of extensional oscillations in the (solid) beam, $\mathcal{T}^*_{\text{s}}=l^*_{\text{flexible}}\sqrt{\rho^*_{\text{s}}/E^*_{\text{eff}}}$, to the timescale $\mathcal{T}^*$ used in the nondimensionalization of the equations. Being *in vacuo* we simply choose $\mathcal{T}^*=\mathcal{T}^*_{\text{s}}$, giving $\Lambda=1$. The parameter Λ^2 may also be interpreted as the nondimensional beam density, thus by setting $\Lambda=0$ we may ignore beam inertia.

For free oscillations *in vacuo* the traction $\mathbf{T}=\mathbf{0}$ in Eqn. (1). However, in order to deform the beam into an initial configuration from which it is released an external traction is applied in the steady form of Eqn. (1), as described in 'Boundary and initial conditions'.

For the 2-d beam model a pair of Lagrangian coordinates [see Fig. 1(c)] parameterize the Eulerian position vector, $\mathbf{R}(\xi^1,\xi^2,t)$, and the PVD becomes

$$\int\left\{\sigma^{ij}\,\delta\gamma_{ij}-\left(\mathbf{F}-\Lambda^2\frac{\partial^2\mathbf{R}}{\partial t^2}\right)\cdot\delta\mathbf{R}\right\}\,dv-\oint_{A_{tract}}\mathbf{T}\cdot\delta\mathbf{R}\,dA=0, \tag{6}$$

where σ^{ij} is the (symmetric) second Piola-Kirchhoff stress tensor, γ_{ij} is the Green strain tensor, $\mathbf{F}$ is the body force per unit volume, dv is the differential unit of volume in the undeformed configuration, and A_{tract} is the deformed surface area over which acts the traction $\mathbf{T}$.

Since we do not include the effects of gravity $\mathbf{F}=\mathbf{0}$ and again the traction is $\mathbf{T}=\mathbf{0}$ in the unsteady solution. We choose the same characteristic length as for the 1-d beam model, but the stresses and tractions are nondimensionalized on the 'real' (i.e. 3-d) elastic modulus, $\mathcal{S}^*=E^*$, thus

$$\Lambda=\frac{l^*_{\text{flexible}}}{\mathcal{T}^*}\sqrt{\frac{\rho^*_{\text{s}}}{E^*}}. \tag{7}$$

As before the equations are nondimensionalized on the natural timescale of the solid so $\Lambda^2=1$.

FSI When the beam is immersed in the viscous channel flow we choose the height of the channel as the characteristic length, $\mathcal{L}^*=H^*$, the mean inlet velocity as the characteristic velocity, $\mathcal{U}^*=U^*$, the natural timescale of the fluid flow as the characteristic time, $\mathcal{T}^*=\mathcal{T}^*_{\text{f}}=H^*/U^*$, and use the viscous scale to define a characteristic pressure, $\mathcal{P}^*=\mu^*U^*/H^*$. The fluid flow is then governed by the nondimensional Navier-Stokes equations

$$\text{Re}\left(\text{St}\frac{\partial u_i}{\partial t}+u_j\frac{\partial u_i}{\partial x_j}\right)=-\frac{\partial p}{\partial x_i}+\frac{\partial}{\partial x_j}\left[\left(\frac{\partial u_i}{\partial x_j}+\frac{\partial u_j}{\partial x_i}\right)\right], \tag{8}$$

and nondimensional continuity equation

$$\frac{\partial u_i}{\partial x_i}=0, \tag{9}$$

where $\text{Re}=\rho^*_{\text{f}}U^*H^*/\mu^*$ and $\text{St}=(H^*/U^*)/\mathcal{T}^*=1$ are the Reynolds number and Strouhal number, respectively.

For the 1-d beam immersed in fluid flow the PVD is as per Eqn. (1) but the traction vector is the summed pressure and viscous loads of the fluid on its 'top' and 'bottom' faces,

$$T_i=Q\left\{\left[p\big|_{\text{top}}\hat{N}_i^{[\text{top}]}-\left(\frac{\partial u_i}{\partial x_j}+\frac{\partial u_j}{\partial x_i}\right)\bigg|_{\text{top}}\hat{N}_j^{[\text{top}]}\right]+\left[p\big|_{\text{bottom}}\hat{N}_i^{[\text{bottom}]}-\left(\frac{\partial u_i}{\partial x_j}+\frac{\partial u_j}{\partial x_i}\right)\bigg|_{\text{bottom}}\hat{N}_j^{[\text{bottom}]}\right]\right\}, \tag{10}$$

for $i=1,2$, where $\hat{\mathbf{N}}^{[top]}$ and $\hat{\mathbf{N}}^{[bottom]}$ are the outer unit normals on the top and bottom faces of the deformed beam. The nondimensional parameter

$$Q=\frac{\mu^*U^*}{E^*_{\text{eff}}H^*} \tag{11}$$

is the ratio of the fluid pressure scale, μ^*U^*/H^* $(=\mathcal{P}^*)$, used to nondimensionalize the Navier-Stokes equations, to the beam's effective elastic modulus, E^*_{eff} $(=\mathcal{S}^*)$, used to nondimensionalize the PVD equation. Q therefore indicates the strength of the fluid-structure interaction. In particular, if $Q=0$ the beam deformation is not affected by the fluid flow.

For the fluid-immersed 2-d beam the traction vector is

$$T_i=Q\left[p\hat{N}_i-\left(\frac{\partial u_i}{\partial x_j}+\frac{\partial u_j}{\partial x_i}\right)\hat{N}_j\right] \tag{12}$$

where

$$Q=\frac{\mu^*U^*}{E^*H^*}. \tag{13}$$

Note that when the beam is immersed in channel flow the solid mechanics timescale ratio can be expressed as $\Lambda^2 = (\rho_s^*/\rho_f^*)\mathrm{Re}\,\mathrm{St}^2 Q$.

Constitutive law For 'slender' beam geometries large bending deflections do not create large strains, so a linearized relation between stresses and strains is appropriate. In our constitutive equation we form the tensor of elastic coefficients with the deformed metric tensor rather than the undeformed one. This yields a geometrically nonlinear formulation [e.g., Equations (4a,b) in the 1-d beam model] as the strain depends nonlinearly on the displacements, capturing the kinematics of the deformation exactly for arbitrarily large displacements and rotations, though for small strains the difference between this and a linear theory is negligible.

As the thickness of the beam increases relative to its length the strains on the top and bottom surfaces become significant at large bending deflections. Which constitutive equation one ought to use in the large strain regime is not straightforward and depends on the specific material being modeled. The work presented here focuses on beams slender enough for this not to be an issue, although the capability exists to use a full nonlinear constitutive relation (e.g., Neo-Hookean, Mooney-Rivlin).

Boundary and initial conditions The 1-d and 2-d beams are clamped at the upstream end and free at the downstream end. When fluid-immersed no slip conditions are applied on all walls. For the flexible walls this is given by

$$\mathbf{u} = \mathrm{St}\frac{\partial \mathbf{R}(\xi,t)}{\partial t}. \tag{14}$$

for the 1-d beam and

$$\mathbf{u} = \mathrm{St}\,\frac{\partial \mathbf{R}(\xi_{[\mathrm{top,tip,bottom}]},t)}{\partial t} \tag{15}$$

for the 'top', 'tip' and 'bottom' surfaces of the 2-d beam (parameterized by local Lagrangian coordinates). The two inlets have a parabolic velocity profile and the outflow is parallel.

For a linear Euler-Bernoulli cantilevered beam of length l and flexural rigidity B the n^{th} eigenmode of amplitude η_0 is described by a vertical displacement profile $\eta_n(x)$, which may be produced by applying the following distributed load

$$B\nabla^4\eta_n(x) = B\frac{\eta_0}{2}\left(\frac{\beta_n}{l}\right)^4\left[cosh(\beta_n x/l) - cos(\beta_n x/l) - \frac{S_n}{T_n}\left(sinh(\beta_n x/l) - sin(\beta_n x/l)\right)\right]; \tag{16}$$

$B = Eh^3/[12(1-\nu^2)]$ is the flexural rigidity of the beam, $S_n = \cosh(\beta_n) + \cos(\beta_n)$, $T_n = \sinh(\beta_n) + \sin(\beta_n)$ and β_n satisfy $\cos(\beta_n)\cosh(\beta_n) = -1$ (e.g., $\beta_2 = 4.6941$). In the present work we apply $\mathbf{T} + (0, B\nabla^4\eta_2(\xi))$ to the 1-d beam and $\mathbf{T} + (0, B\nabla^4\eta_2(\xi_{\mathrm{top}}))$ to the 2-d beam as initial conditions in the steady problem, with no flow at the inlets for the fluid-immersed cases.

Numerical implementation

The problem is formulated using the open-source finite-element library `oomph-lib` [10, 11]. We use two-node Hermite beam elements for the 1-d beam and nine-node quadrilateral displacement-based solid mechanics (PVD) elements for the 2-d equivalent. Nine-node quadrilateral Taylor-Hood elements are used for the fluid. Timestepping is performed using a Newmark scheme for the solid and a BDF scheme for the fluid. The FSI problem is discretized monolithically and the Newton-Raphson method is used to solve the nonlinear system of equations (specified by the global Jacobian matrix and the global residual vectors), employing the SuperLU direct linear solver within the Newton iteration.

The external traction used to produce the second eigenmode displacement of the beam is applied incrementally over a series of steady solves. The external traction is then removed and the beam is free to oscillate. In the fluid-immersed case the flow is ramped up from zero over a period of 20 time steps. We have tested our code at various mesh densities and timestep sizes, and employed `oomph-lib`'s adaptive mesh refinement capabilities; e.g., see Fig. 5(b).

Parameter values

To appreciate the physical scales of the problem we specify the input parameters in dimensional form and then derive their associated nondimensional quantities. To facilitate comparison with the more familiar linear Euler-Bernoulli formulation of the structural mechanics we choose the same channel and beam parameter values as the original 'Plate 2' simulations in [7], except here the mean inlet velocity is an order of magnitude smaller. Additionally, both for our 1-d and 2-d beams, we require a thickness (h), which we choose such that $h^*/l^*_{\mathrm{flexible}} = 1/32$, and a Poisson's ratio (ν), which we obtain from [6]. This set of dimensional parameter values are summarized in Table 1 and form the reference for subsequent parametric variations. The corresponding values of the important nondimensional parameters required to set up the finite element problems (*in vacuo* and FSI) in `oomph-lib` are summarized in Table 2.

RESULTS

In the results that follow all parameter values are as per Tables 1 and 2 unless stated otherwise.

TABLE 1. DIMENSIONAL PARAMETER VALUES.

Parameter	Value	Description
L^*	40.5 mm	Length of channel
H^*	5.0 mm	Height of channel
l^*_{rigid}	6.0 mm	Length of rigid central wall
l^*_{flexible}	8.0 mm	Length of flexible plate
h^*	0.25 mm	Thickness of flexible plate
ρ^*_{f}	1.1774 kg/m^3	Density of fluid
μ^*	1.98×10^{-5} kg/(m·s)	Dynamic viscosity of fluid
ν	0.3333	Poisson's ratio of solid
$\rho^*_{\text{s}}h^*$	0.0248 kg/m^2	Mass per unit area of solid
B^*	1.87×10^{-8} N·m	Flexural rigidity of flexible plate
U^*	0.08488 m/s	Mean inlet velocity
η^*_0	0.08 mm	Amplitude of initial flexible plate eigenmode displacement

TABLE 2. NONDIMENSIONAL PARAMETER VALUES.

Case	Parameter	Value	Description
in vacuo	Λ^2	1	Solid-mechanics timescale ratio
FSI	Re	25.2	Reynolds number
	St	1	Strouhal number
	Q	1.05×10^{-6}	FSI parameter
	$\rho^*_{\text{s}}/\rho^*_{\text{f}}$	84.2	Solid-to-fluid density ratio
	Λ^2	1.98×10^{-3} (1-d), 2.23×10^{-3} (2-d)	Solid-mechanics timescale ratio

In vacuo

Since our initial condition for the channel flow problem involves an eigenmode displacement we first verify the structural codes against linear Euler-Bernoulli theory. We begin with the 1-d beam code.

The bold curve in Fig. 2 shows the second mode displacement profile corresponding to the applied load of $\mathbf{T}_{\text{ext}}$, as predicted by the linear theory; the nondimensional y coordinate is normalized by the amplitude of the displacement η_0

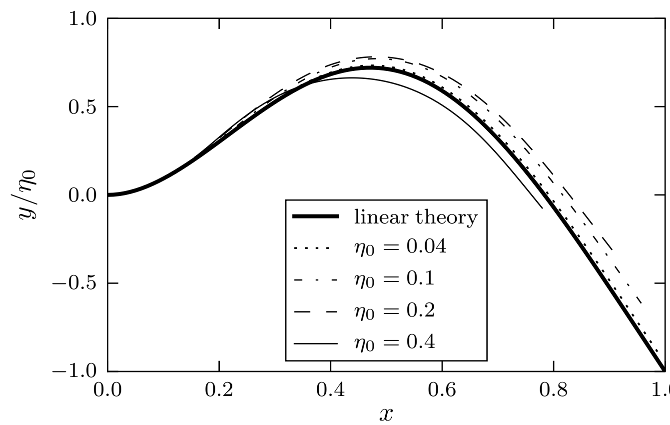

FIGURE 2. APPROXIMATIONS OF THE SECOND IN VACUO LINEAR EIGENMODE AT DIFFERENT AMPLITUDES η_0 FOR THE 1-D PLATE.

($= \eta^*_0/l^*_{\text{flexible}}$). For a finite length 1-d beam one would expect a departure from this profile for increasing amplitudes as the curvature becomes more prominent. This is exactly what is observed in the four remaining curves corresponding to η_0 = 0.04, 0.1, 0.2 and 0.4. For smaller η_0 the displacement predicted by the numerical code and the linear theory become indistinguishable, verifying the 1-d code for steady static solutions.

Figure 3 demonstrates what happens when the previous applied load is removed and the beam allowed to oscillate freely for the (a) $\eta_0 = 0.04$ and (b,c) $\eta_0 = 0.2$ cases. Consider Fig. 3(a). The beam begins from the profile indicated by the bold green curve ($t^* = 0$, corresponding to the dotted curve in Fig. 2) and the ensuing oscillations have the mode shape described by the series of black curves; the final snap shot at $t^* = 1.2$ sec is given by the bold red curve. Since the amplitude is sufficiently small the mode closely matches the well-known shape predicted by linear theory [e.g., see [6], Fig. 2(b)]. Figure 3(b) shows the analogous result for larger amplitude oscillations that, as expected, deviate significantly from the linear mode. A time trace of the vertical position of the beam tip from Fig. 3(b) is depicted in Fig. 3(c). To verify the 1-d code for unsteady solutions we examine the eigenmode frequency. Figure 4 shows the ratio of the numerical results to the theoretical prediction over a range of amplitudes for the second and fourth modes. As the amplitude approaches the linear regime there is a convergence to the linear theory ($\omega/\omega_n \rightarrow 1$).

Adding a second dimension to the beam allows for stress variation across the thickness. Figure 5(a) demonstrates the compressive (blue) and tensile (red) stresses of the second eigenmode. In order to resolve the large stress gradients at the clamped end the mesh has automatically refined itself using the quad-tree procedure, as shown in Fig. 5(b). Analysis of the eigenmode static profiles and oscillation frequencies reveals the same behavior demonstrated for the 1-d beam in

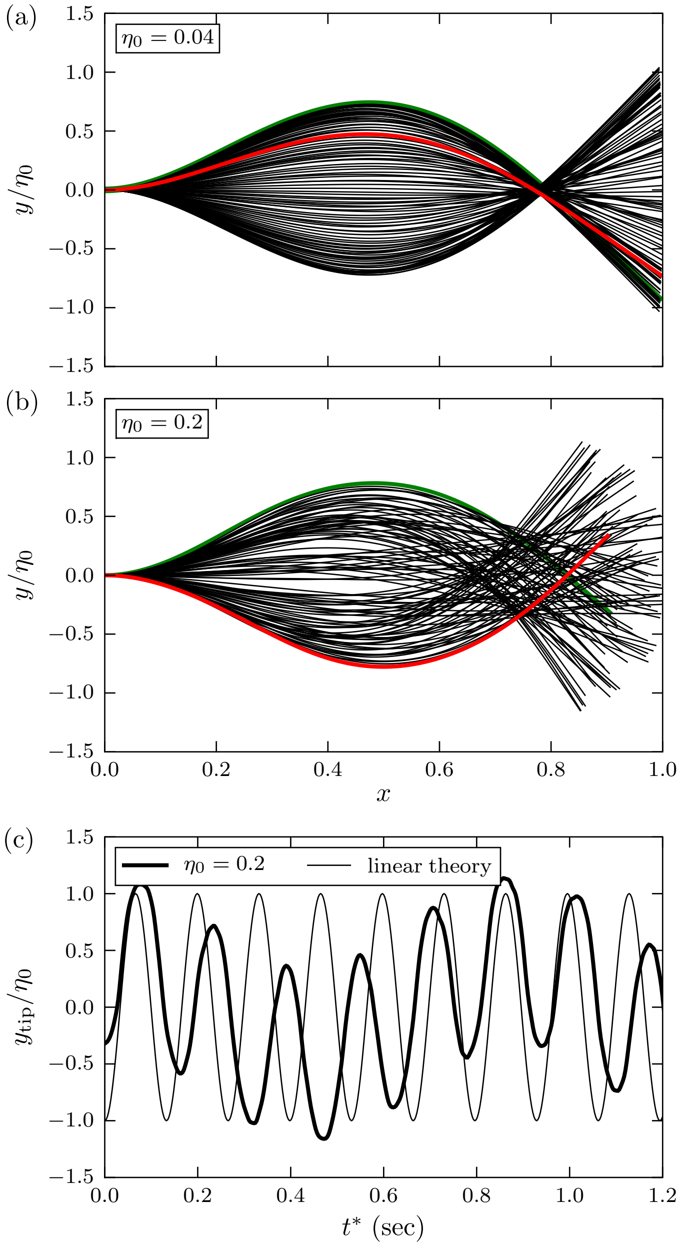

FIGURE 3. (a,b) DEMONSTRATION OF THE INFLUENCE OF AMPLITUDE ON MODE SHAPE AND (c) TIP POSITION FOR THE 1-D PLATE MODEL IN VACUO.

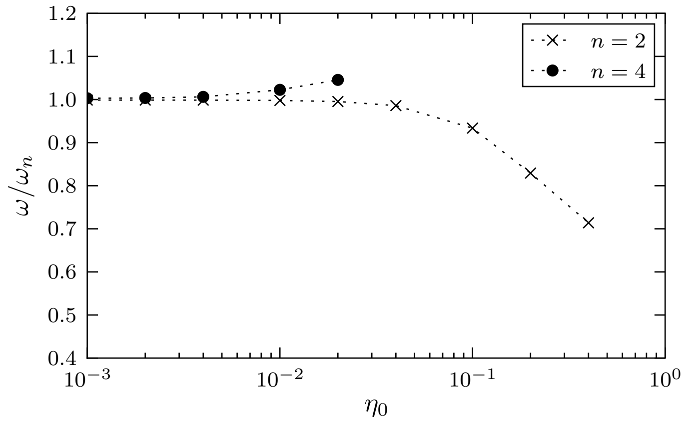

FIGURE 4. VERIFICATION OF THE DYNAMIC RESPONSE OF THE 1-D BEAM IN VACUO—CONVERGENCE OF MODE FREQUENCY ω TO THE LINEAR THEORY AT SMALL AMPLITUDES.

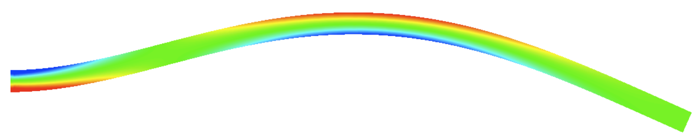

(a) stress field

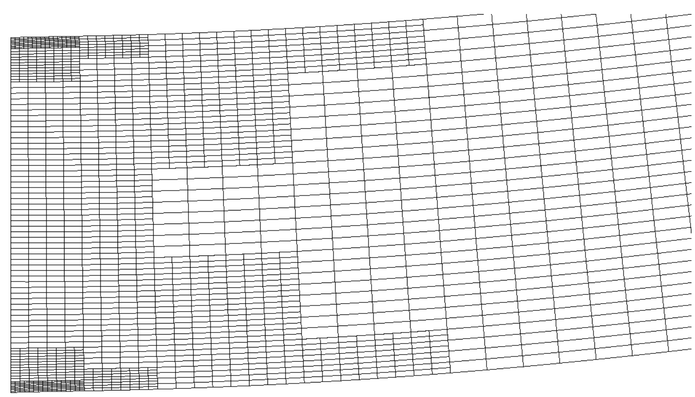

(b) mesh

FIGURE 5. (a) STRESS FIELD IN THE 2-D BEAM IN VACUO RANGING FROM COMPRESSIVE (BLUE) TENSILE (RED); (b) DEMONSTRATION OF MESH ADAPTING AROUND STRESS CONCENTRATION AT THE CLAMPED END.

the limit of small amplitudes (Figures 2–4) provided that the beam thickness-to-length ratio is also small, with increasing deviation from this behavior at larger ratios. The 2-d beam code has also been verified previously using the case of a uniform applied transverse load by comparing with the theoretical St Venant's solution for the stress field (see *http://oomph-lib.maths.man.ac.uk/doc/solid/airy_cantilever/html/index.html*).

FSI

Having established the credibility of the structural models we now couple these to the fluid model and investigate their interaction. Once again beginning with the 1-d beam, consider Fig. 6. Figure 6(a) shows the initial mesh with the central rigid wall drawn in red and the beam in blue. This structured mesh deforms according to the movements of the beam. Plotted in

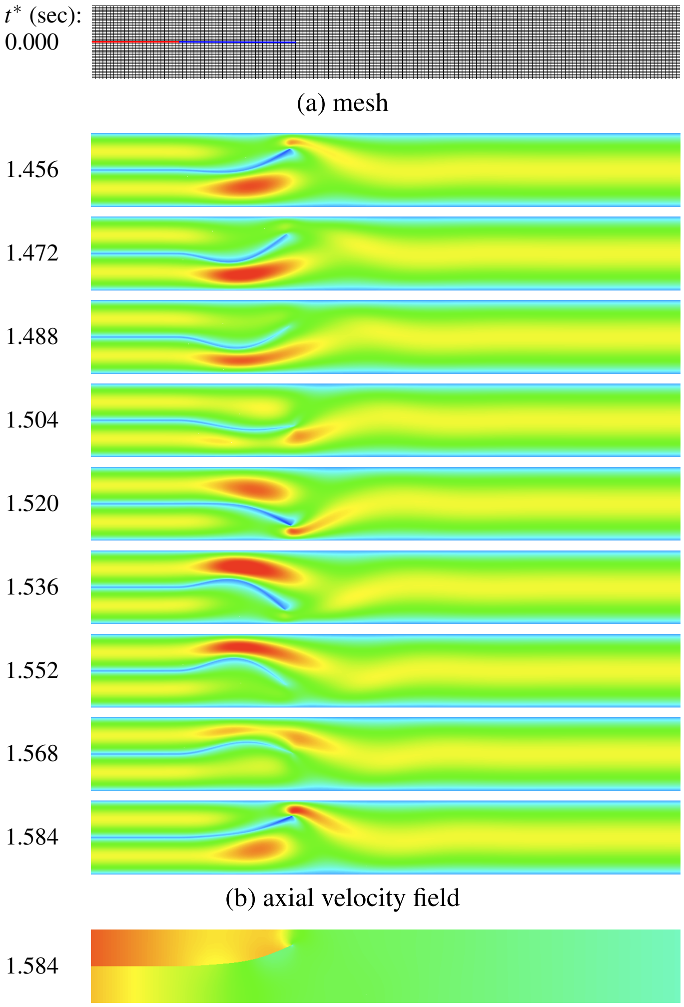

(a) mesh

(b) axial velocity field

(c) pressure field

FIGURE 6. A LARGE-AMPLITUDE UNSTEADY OSCILLATION IN THE 1-D PLATE IN CHANNEL FLOW. FIELD VARIABLES COLORED BLUE-LOW TO RED-HIGH.

Fig. 6(b) are a series of axial velocity (u_1) fields at consecutive time steps showing the beam undergoing an oscillation, and Fig. 6(c) shows the corresponding pressure field at the last time step. This simulation begins in a mode 2 configuration with a displacement amplitude of $\eta_0 = 0.01$, which grows exponentially in time through a series of oscillations, reaching some twenty times that amplitude by the cycle depicted in Fig. 6.

The analogous plots for the 2-d beam FSI model are shown in Fig. 7, although the magnitude rather than axial component of velocity is plotted. The beam thickness ratio is again 1/32 but this now relates to a second geometrical dimension rather than simply as a means of approximating the contribution of flexural rigidity. For brevity we now focus on this rather than the 1-d beam FSI model noting that we observe similar behavior in both. Although Fig. 7 clearly depicts a large-amplitude oscillation one can better appreciate the instability of the system from Fig. 8(a), where the vertical displacement of the tip of the beam centerline has been plotted as it varies in time (bold line); the second *in vacuo* eigenmode from linear theory is also plotted (thin line) to show how the FSI augments the amplitude and frequency of the structural oscillations. A flutter instability is present as evident by the amplitude growth of the oscillations. The reduction in oscillation frequency by 4% compared to the *in vacuo* linear theory is largely accounted for by the fluid traction. By reducing the inlet velocity by an order of magnitude the same initial conditions produce oscillations that decay very rapidly, as demonstrated in Fig. 8(b). This shows the existence of a critical flow speed (or Re) for flutter onset.

The stability trend with inlet velocity magnitude can be gleaned from Fig. 9 in which the centerline tip amplitude is plotted in logarithmic scale against time. The curve with '$\times$' markers denotes a simulation for which the FSI is switched off by setting $Q = 0$; i.e., the beam does not 'feel' the fluid traction and so is able to oscillate freely, effectively serving as a mechanism for deforming a time-dependent fluid domain. The amplitude remains constant at the initial value, as would be expected. Using this as a neutral stability reference we can interpret the remaining cases for which Q assumes its natural value. As the inlet velocity is reduced from $10U$ down to $U/10$ the amplitude growth rate reduces, eventually becoming less than unity when stability is achieved. Linearly interpolating the growth rates predicts a critical Re of around 4 ($U^* = 0.015$ m/s) for this channel geometry. The curves denoted by '$2U$' (doubled inlet velocity) and '$U, 2H$' (doubled channel width) have the same Re but the former is unstable while the latter is stable. This is because increasing the channel width reduces the Bernoulli effect between the beam and the channel walls.

Space limitations prevent us from presenting a detailed stability analysis but to demonstrate the capability to do so, we include results for a beam of double thickness but same mass per unit area ('$U, 2h$', Fig. 8), suggesting beam thickness may be a stabilising factor, and a beam of 10 times the density ('$U, 10\rho_s$'), which suggests that a uniform increase in inertia may be destabilising. The tip of a thick beam is a bluff body to the viscous flow field, as shown in Fig. 10, and vortices shed due to the low-pressure region that develops behind the tip face may play a rôle in the stability characteristics of the beam flutter. The additional inertia also affects the mode shape of oscillations as illustrated in the centerline plots of Fig. 11—the denser beam in (b) bends more prominently in the mid-section than that in (a).

Conclusion

We have presented a model of a finite-thickness cantilevered flexible plate interacting with a viscous channel flow. A geo-

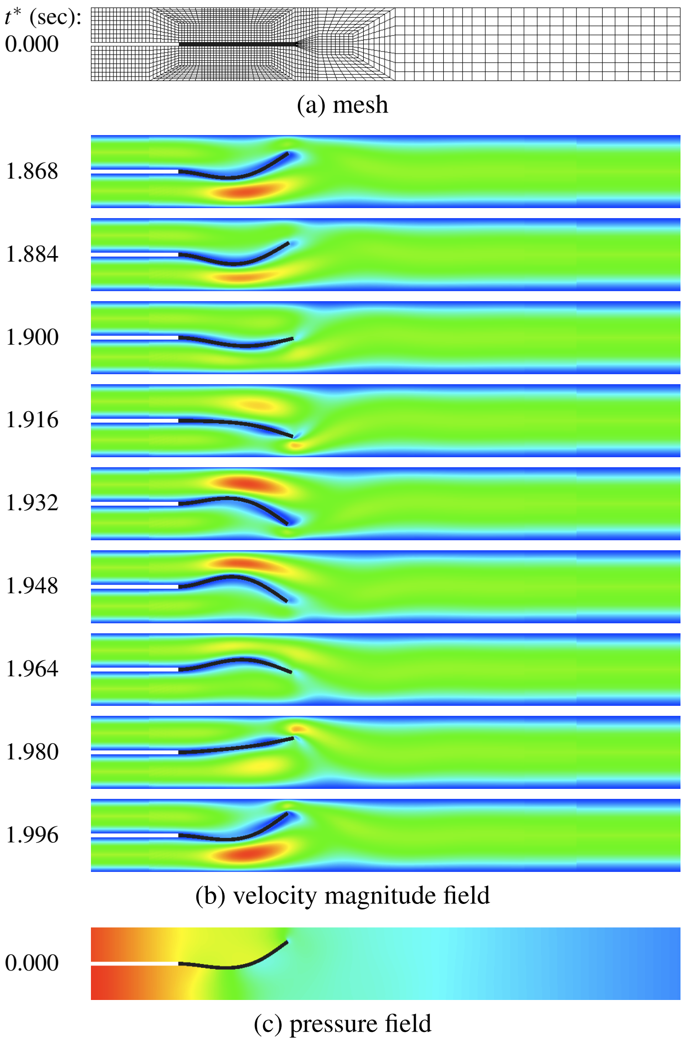

FIGURE 7. 2-D BEAM IN CHANNEL FLOW, ANALOGOUS PLOTS TO FIG. 6.

metrically nonlinear formulation of the solid mechanics was employed. This model was developed using `oomph-lib`, an open-source finite-element library. We have demonstrated both stable and unstable motions of the flexible plate with the latter involving large-amplitude flutter-type oscillations. This work provides the infrastructure for a more anatomically accurate analysis of the mechanisms underlying obstructive breathing disorders.

Acknowledgement

We acknowledge the support of both the Australian Research Council through the project DP0559408 and the WA State Centre of Excellence in eMedicine in the continuing project 'Airway Tomography Instrumentation'.

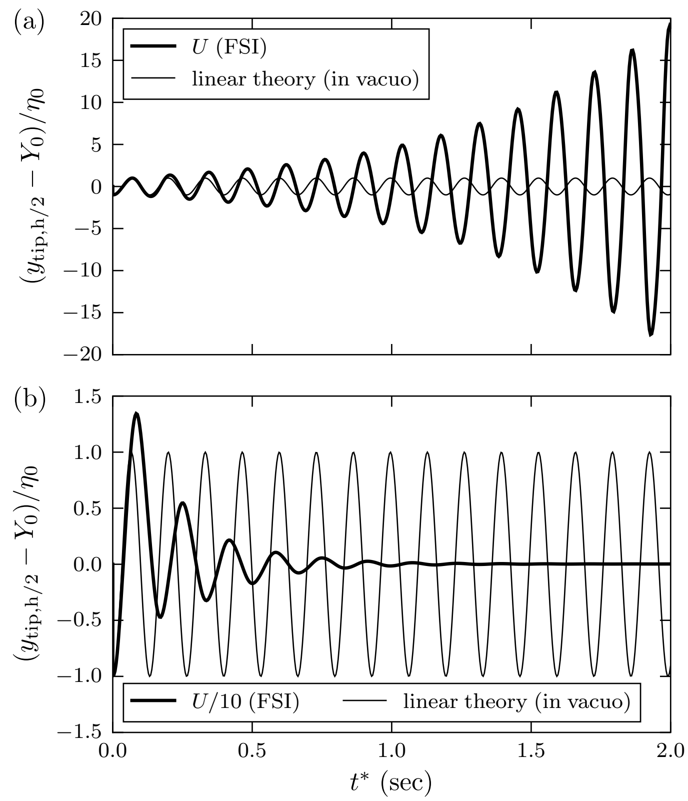

FIGURE 8. FSI-RESPONSES: TRACES OF THE CENTER OF THE 2-D PLATE TIP SHOWING (a) UNSTABLE AND (b) STABLE OSCILLATIONS.

REFERENCES

[1] Huang, L., Quinn, S. J., Ellis, P. D. M., and Ffowcs Williams, J. E., 1995. "Biomechanics of snoring". *Endeavour,* ***19***(3), pp. 96–100.

[2] Huang, L., 1995. "Flutter of cantilevered plates in axial flow". *Journal of Fluids and Structures,* ***9***(2), pp. 127–147.

[3] Aurégan, Y., and Depollier, C., 1995. "Snoring: linear stability analysis and in-vitro experiments". *Journal of Sound and Vibration,* ***188***, pp. 39–53.

[4] Guo, C. Q., and Païdoussis, M. P., 2000. "Stability of rectangular plates with free side-edges in two-dimensional inviscid channel flow". *Journal of Applied Mechanics,* ***67***, pp. 171–176.

[5] Howell, R. M., Lucey, A. D., Carpenter, P. W., and Pitman, M. W., 2009. "Interaction between a cantilevered-free flexible plate and ideal flow". *Journal of Fluids and Structures,* ***25***, pp. 544–566.

[6] Balint, T. S., and Lucey, A. D., 2005. "Instability of a cantilevered flexible plate in viscous channel flows". *Journal of Fluids and Structures,* ***20***, pp. 893–912.

[7] Tetlow, G. A., and Lucey, A. D., 2009. "Motions of a cantilevered flexible plate in viscous channel flow driven by a constant pressure drop". *Communications In Numerical Methods In Engineering,* ***25***, pp. 463–482.
[8] Tang, L., Païdoussis, M. P., and Jiang, J., 2009. "Cantilevered flexible plates in axial flow: Energy transfer and the concept of flutter mill". *Journal of Sound and Vibration,* ***326***, pp. 529–542.
[9] Tang, L., and Païdoussis, M. P., 2007. "On the instability and the post-critical behaviour of two-dimensional cantilevered flexible plates in axial flow". *Journal of Sound and Vibration,* ***305***, pp. 97–115.
[10] Heil, M., and Hazel, A. L., 2006. "oomph-lib – an Object-Oriented Multi-Physics Finite-Element Library". In *Fluid-Structure Interaction*, M. Schafer and H.-J. Bungartz, eds., Lecture Notes on Computational Science and Engineering. Springer, pp. 19–49. `oomph-lib` is available as open-source software at: *http://www.oomph-lib.org*.
[11] Heil, M., Hazel, A. L., and Boyle, J., 2008. "Solvers for large-displacement fluid-structure interaction problems: Segregated vs. monolithic approaches". *Computational Mechanics,* ***43***, pp. 91–101.

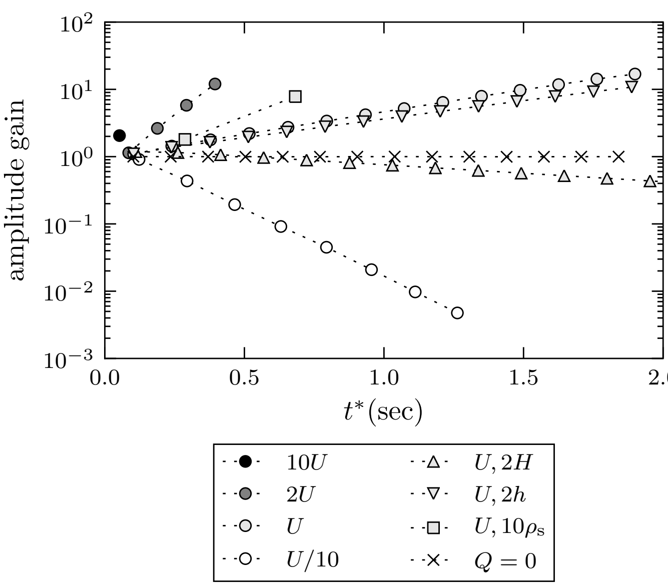

FIGURE 9. GROWTH AND DECAY OF 2-D PLATE OSCILLATIONS FOR DIFFERENT SYSTEM PARAMETERS.

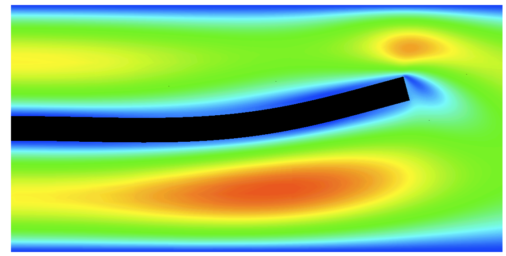

(a) velocity magnitude

(b) pressure

FIGURE 10. ILLUSTRATION OF THE FLOW SEPARATION THAT DEVELOPS DOWNSTREAM OF THE 2-D PLATE TIP FACE WHEN PLATE THICKNESS BECOMES LARGE.

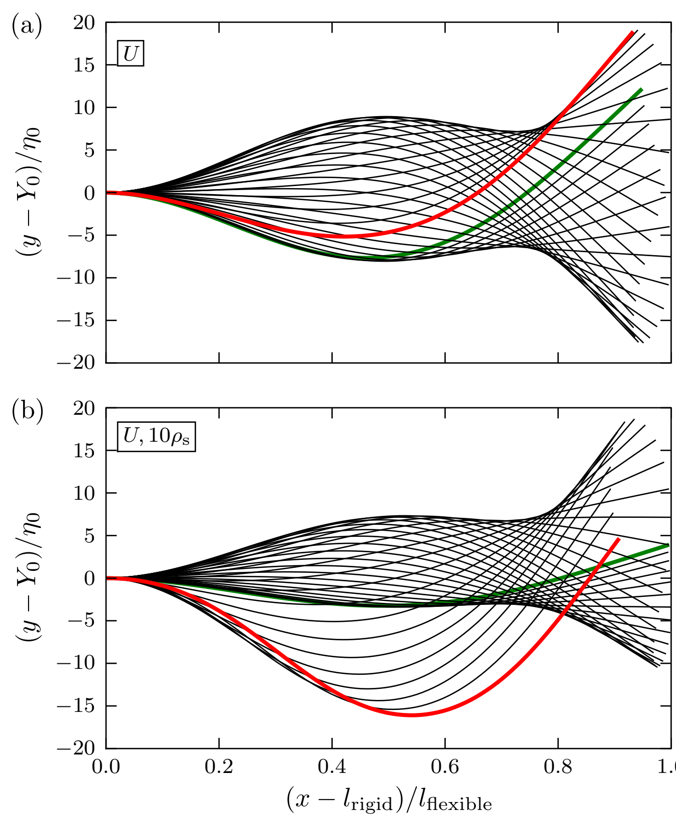

FIGURE 11. THE INFLUENCE OF INERTIA ON (CENTERLINE) MODE SHAPE IN THE 2-D PLATE IN CHANNEL FLOW.